Atomistic simulation of barocaloric effects

Claudio Cazorla[1,*]

[1] *Departament de Física, Universitat Politècnica de Catalunya, Campus Nord B4-B5, Barcelona 08034, Spain*

Due to critical environmental issues there is a pressing need to switch from current refrigeration methods based on compression of greenhouse gases to novel solid-state cooling technologies. Solid-state cooling capitalizes on the thermal response of materials to external fields named "caloric effect". The barocaloric (BC) effect driven by hydrostatic pressure is particularly promising from a technological point of view since typically presents larger cooling potential than other caloric variants (e.g., magnetocaloric and electrocaloric effects driven by magnetic and electric fields, respectively). Atomistic simulation of BC effects represents an efficient and physically insightful strategy for advancing solid-state cooling by complementing, and in some cases even guiding, experiments. Atomistic simulation of BC effects involves approaches ranging from computationally inexpensive force fields to computationally very demanding, but quantitatively accurate, first-principles methods. Here, we review several methods and strategies involved in atomistic simulation of BC effects like the quasi-harmonic approximation and direct/quasi-direct estimation approaches. The Chapter finalizes with a collection of case studies in which some of these methods were employed to simulate and predict original BC effects.

I. INTRODUCTION

When the isothermal entropy changes associated with fluctuations in the electric, magnetic and structural properties of materials are large, $|\Delta S_T| \sim 10$–$100\ \mathrm{kJK^{-1}kg^{-1}}$, these may render sizable caloric effects (e.g., adiabatic temperature changes of $|\Delta T_S| \sim 1$–10 K). Solid-state cooling is an environmentally friendly, highly energy-efficient, and highly scalable technology that exploits caloric effects in materials for refrigeration purposes [1–8]. By applying external fields on caloric materials it is possible to achieve reversible temperature shifts that can be integrated in cooling cycles and do not involve the use of greenhouse gases. Materials undergoing abrupt structural phase transitions under small hydrostatic pressure are specially well suited for solid-state cooling applications based on the barocaloric (BC) effect [1–3].

The magnitude of BC effects can be estimated accurately with theoretical and atomistic simulation methods. Computer simulations can be used to rationalize the origins of experimentally observed BC phenomena since the materials and pressure-induced phase transitions of interest can be accessed at the atomic scale under controlled conditions. Moreover, from a resources point of view computer simulations are inexpensive. For instance, by using open-source software and modest computational resources it is possible, in some cases, to simulate complex BC effects and assess the magnitude of the accompanying isothermal entropy and adiabatic temperature shifts. Thus, modeling of BC effects can be done systematically in order to complement, and in some cases also guide, the experiments.

The reliability of computer simulations, however, depends strongly on the simplifications made on the adopted structural and interatomic interaction models. Typically, increasing the reliability of the structural models comes at the expense of reducing the accuracy in the description of the interatomic forces (due to practical computational limitations). For instance, if the simulation approach to be employed is accurate first-principles methods most calculations are likely to be performed at zero temperature by considering perfectly ordered atomic structures. Such simulation conditions obviously differ from the actual experimental conditions. On the other hand, to simulate BC effects directly at finite temperatures for realistic systems containing crystalline defects and/or other inhomogeneities one should use computationally inexpensive interatomic modeling techniques, which may suffer from transferability issues and in general have modest predictive power. Fortunately, there are well-established simulation strategies that allow to achieve a suitable balance between computational accuracy and model reliability and can be used to obtain physically meaningful results.

In this Chapter, we review general computational techniques based on atomistic simulation methods that can be used to theoretically estimate and predict BC effects. We start by briefly describing genuine first-principles methods, like density functional theory, and other practical approaches that allow to describe the interactions between atoms in materials, namely, classical interatomic and machine learning potentials. Next, several computational techniques that allow to describe phase transitions and estimate thermodynamic properties of materials (e.g., free energies and entropies) are summarized (e.g., the quasi-harmonic approximation and thermodynamic integration methods). Subsequently, different simulation strategies that can be employed for indirect, quasi-direct and direct evaluation of BC effects are succinctly explained. We finalize the Chapter by providing some representative examples in which atomistic simulation methods have been used to predict original BC effects in families of materials that are technologically relevant, namely, fast-ion conductors [4, 9–11], complex

* claudio.cazorla@upc.edu

hydrides [12] and multiferroic perovskite oxides [13 and 14]. This Chapter is addressed to both experienced computational materials scientists with an interest on caloric effects and solid-state cooling as well as to novice researchers wanting to learn modeling techniques of phase transitions and free-energy methods.

II. MODELING OF ATOMIC INTERACTIONS

The fundamentals of density functional theory (DFT), a first-principles approach widely used in condensed-matter and materials science, and classical interatomic potentials are briefly reviewed next. The latter interatomic interactions modeling approach is approximate and typically rely on the results of accurate first-principles methods (also called *ab initio*) like DFT. On the other hand, the computational cost of DFT methods is several orders of magnitude higher than that of classical interatomic potentials, hence in many occasions first-principles methods may not be directly employed in the study of BC effects. Machine learning potentials are also succinctly described since they constitute a modern atomistic modeling technique in the middle way between DFT and classical potential approaches both in terms of accuracy and computational expense.

A. *Ab initio* methods

In solids, the dynamics of the electrons and nuclei can be decoupled to a good approximation because their respective masses differ by several orders of magnitude. The wave function of the corresponding many-electron system, $\Psi(\mathbf{r}_1, \mathbf{r}_2, ..., \mathbf{r}_N)$, therefore can be determined by solving the Schrödinger equation corresponding to the non-relativistic Born-Oppenheimer Hamiltonian:

$$H = -\frac{1}{2}\sum_i \nabla_i^2 - \sum_I \sum_i \frac{Z_I}{|\mathbf{R}_I - \mathbf{r}_i|} + \frac{1}{2}\sum_i \sum_{j\neq i} \frac{1}{|\mathbf{r}_i - \mathbf{r}_j|} \ , \quad (1)$$

where Z_I are the nuclear charges, $\mathbf{r}_i$ the positions of the electrons, and $\mathbf{R}_I$ the positions of the nuclei (considered to be fixed). In real materials, Ψ is a complex mathematical function that in most cases is unknown. At the heart of any first-principles method is to find a good approximation for Ψ, or an equivalent quantity (e.g., the electronic density), that is manageable enough to perform calculations. Examples of *ab initio* methods include density functional theory (DFT), Møller-Plesset perturbation theory (MP2), the coupled-cluster method with single, double and perturbative triple excitations [CCSD(T)], and quantum Monte Carlo (QMC), to cite just a few. Among these techniques, DFT methods are frequently applied to the study of materials and pressure-induced phase transitions hence for this reason we summarise their foundations in what follows.

In 1965, Kohn and Sham developed a pioneering theory to effectively calculate the energy and properties of many-electron systems without the need of explicitly knowing Ψ [15 and 16]. The main idea underlying this theory, called density functional theory (DFT), is that the exact ground-state energy, E, and electron density, $n(\mathbf{r})$, can be determined by solving an effective one-electron Schrödinger equation of the form:

$$H_{\rm KS}\Psi_{i\sigma} = \epsilon_{i\sigma}\Psi_{i\sigma} \ , \quad (2)$$

where $H_{\rm KS}$ is the Kohn-Sham Hamiltonian, index i labels different one-electron orbitals and σ different spin states. The KS Hamiltonian can be expressed as:

$$H_{\rm KS} = -\frac{1}{2}\nabla^2 + V_{ext}(\mathbf{r}) + \int \frac{n(\mathbf{r}')}{|\mathbf{r} - \mathbf{r}'|} d\mathbf{r}' + V_{xc}(\mathbf{r}) \ , \quad (3)$$

where

$$n(\mathbf{r}) = \sum_{i\sigma} |\Psi_{i\sigma}(\mathbf{r})|^2 \ , \quad (4)$$

V_{ext} represents an external field and $V_{xc}(\mathbf{r}) = \delta E_{xc}/\delta n(\mathbf{r})$ is the exchange-correlation potential.

The exchange-correlation energy has a purely quantum mechanical origin and can be defined as the interaction energy difference between a quantum many-electron system and its classical counterpart. Despite E_{xc} represents a relatively small fraction of the total energy, this contribution is extremely crucial for all materials and molecules because it acts directly on the bonding between atoms. In general, $E_{xc}[n]$ is unknown and needs to be approximated. This is the only source of fundamental and uncontrollable errors in DFT methods. In standard DFT approaches, $E_{xc}[n]$ typically is approximated with the expression:

$$E_{xc}^{\rm approx}[n] = \int \epsilon_{xc}^{\rm approx}(\mathbf{r}) n(\mathbf{r}) d\mathbf{r} \ , \quad (5)$$

where $\epsilon_{xc}^{\rm approx}$ is made to depend on $n(\mathbf{r})$, $\nabla n(\mathbf{r})$, and/or the electronic kinetic energy $\tau(\mathbf{r}) = \frac{1}{2}\sum_{i\sigma} |\nabla \Psi_{i\sigma}(\mathbf{r})|^2$. Next, we summarise the basic aspects of the most popular $E_{xc}[n]$ functionals employed in modeling of materials and phase transitions.

In local approaches (e.g., local density approximation –LDA–), $E_{xc}^{\rm approx}$ in Eq.(5) is calculated by considering the exchange-correlation energy of an uniform electron gas with density $n(\mathbf{r})$, ϵ_{xc}^{unif}, which is known exactly from quantum Monte Carlo calculations [17 and 18]. In order to deal with the non-uniformity of real electronic systems, the space is partitioned into infinitesimal volume elements that are considered to be locally uniform. In semi-local approaches (e.g., generalized gradient approximation –GGA–), E_{xc} is approximated similarly than in local approaches but $\epsilon_{xc}^{\rm approx}$ is made to depend also on

the gradient of $n(\mathbf{r})$ [19 and 20]. Both local and semi-local approximations satisfy some exact E_{xc} constraints and can work notably well for systems in which the electronic density varies slowly over the space (e.g., crystals). An extension of the GGA approach is provided by meta-GGA functionals, in which the non-interacting kinetic energy density is considered also as an energy functional input. An example of this latter type of functionals is the recently proposed meta-GGA SCAN [21 and 22].

Hybrid functionals comprise a combination of non-local exact Hartree-Fock and local exchange energies, together with semi-local correlation energies. The proportion in which both non-local and local exchange densities are mixed generally relies on empirical rules. The popular B3LYP approximation [23], for instance, takes a 20% of the exact HF exchange energy and the rest from the GGA and LDA functionals. Other well-known hybrid functionals are PBE0 [24] and the range-separated HSE06 proposed by Scuseria and collaborators [25]. In contrast to local and semi-local functionals, hybrids describe to some extent the delocalisation of the exchange-correlation hole around an electron hence they partially correct for electronic self-interaction errors (which are ubiquitous in standard DFT) [26]. This technical feature is specially useful when dealing with strongly correlated systems that contain d and f electronic orbitals (e.g., transition-metal oxide perovskites) [27–29].

B. Classical interatomic potentials

Using first-principles methods to describe the interactions between electrons and ions in crystals requires dedicated computational resources. In some cases, the interatomic interactions can be approximated satisfactorily by analytical functions known as classical interatomic potentials or force fields and consequently the simulations can be accelerated dramatically with respect to *ab initio* calculations. Classical interaction models contain a number of parameters that are adjusted to reproduce experimental or *ab initio* data, and their analytical expressions are constructed based on physical knowledge and intuition. The force matching method proposed by Ercolessi and Adams [30] is an example of a classical potential fitting technique that is widely employed in the fields of condensed matter physics and materials science [31–34]. Nonetheless, the ways in which classical interatomic potentials are constructed are neither straightforward nor uniquely defined and the thermodynamic intervals over which they remain reliable are limited.

A typical pairwise interaction model that has been widely employed to simulate materials at finite temperatures is the Coulomb–Buckingham (CB) potential, which adopts the simple form [35–38]:

$$V_{\alpha\beta}(r_{ij}) = A_{\alpha\beta}e^{-\frac{r_{ij}}{\rho_{\alpha\beta}}} - \frac{C_{\alpha\beta}}{r_{ij}^6} + \frac{Z_\alpha Z_\beta}{r_{ij}} \ , \qquad (6)$$

where subscripts α and β represent atomic species in the system, r_{ij} the radial distance between a pair of α and β atoms labelled i and j respectively, Z ionic charges, and A, ρ and C are potential parameters. The CB potential is composed of three different energy contributions. The exponential term accounts for short-range repulsive forces resulting from the interactions between nearby electrons; the second term represents long-range attractive interactions arising from dispersive van der Waals forces; the third term is the usual Coulomb interaction between point charges. In order to describe atomic polarizability effects, "core-shell" modeling can be performed on top of the CB potential. In standard core-shell approaches, each atom is decomposed into a charged core, which interact with others through V_{ij}'s analogous to the expression shown in Eq.(6), and a charged shell that is harmonically bound to the core [36–39].

Some technologically relevant materials (e.g., oxide and hybrid organic-inorganic perovskites) are characterized by a delicate balance between short-range and long-range forces, which may be respectively originated by electronic orbital hybridizations and the Coulomb interactions between permanent electric dipoles and higher-order moments [40]. The simplicity of the pairwise interaction model in Eq.(6) may not be adequate to fully grasp the complexity of such variety of interatomic interactions. Bond-valence (BV) potentials, for instance, represent an improvement with respect to the CB model because they can mimic chemical bonding in complex materials more precisely [41]. (Many other interatomic interaction models going beyond CB exist, like the embedded atom potential [42 and 43] and multibody force fields [31], but for the sake of focus those are not covered here.)

A general BV potential is [44–47]:

$$V_{\rm BV}(r,\theta) = V_{\rm bind}(r) + V_{\rm charge}(r) + V_{\rm rep}(r) + V_{\rm nl}(\theta) \ , \quad (7)$$

where the first term in the right-hand side represents the bond-valence potential energy, the second the Coulomb potential energy, the third the repulsive potential energy, and the fourth an angle potential energy (to prevent unphysically large distortions of covalently connected structural units; for instance, the oxygen octahedra in oxide perovskites and molecular cations in hybrid organic-inorganic compounds).

The bond-valence energy term generally is expressed as:

$$V_{\rm bind}(r) = \sum_{\alpha=1}^{N_s} S_\alpha \sum_{i=1}^{N_\alpha} \mid V_{i\alpha}(r_i) - V_\alpha \mid^{\gamma_\alpha}, \qquad (8)$$

with

$$V_{i\alpha}(r_i) = \sum_{\beta=1}^{N_s} \sum_{j}^{NN} \left(\frac{r_0^{\alpha\beta}}{r_{ij}^{\alpha\beta}} \right)^{C_{\alpha\beta}}, \qquad (9)$$

where N_s represents the number of atomic species in the

system, S_α are fitting parameters, N_α the number of α atoms, V_α the desired atomic valence for ion α, γ_α fitting parameters typically set to 1, j an atomic index that runs over nearest-neighbour (NN) ions, $r_0^{\alpha\beta}$ and $C_{\alpha\beta}$ parameters determined by empirical rules, and $r_{ij}^{\alpha\beta}$ the radial distance between ions i and j.

For the repulsive energy term, $V_{\rm rep}$, the following expression normally is employed:

$$V_{\rm rep}(r) = \epsilon \sum_{\alpha=1}^{N_s} \sum_{i=1}^{N_\alpha} \sum_{\beta=1}^{N_s} \sum_{j=1}^{N_\beta} \left(\frac{B_{\alpha\beta}}{r_{ij}^{\alpha\beta}} \right)^{12} , \qquad (10)$$

where ϵ and $B_{\alpha\beta}$ are fitting parameters. Meanwhile, an harmonic function is used for the angle potential energy that reads:

$$V_{\rm nl}(\theta) = k \sum_{i=1}^{N_{\rm bun}} \left(\theta_{i,x}^2 + \theta_{i,y}^2 + \theta_{i,z}^2 \right) , \qquad (11)$$

where k is a fitting parameter, $N_{\rm bun}$ the number of covalently bonded units in the simulated system (e.g., oxygen octahedral in oxide perovskites and molecular cations in hybrid organic-inorganic compounds), and $\{\theta_{i,\gamma}\}$ the angular degrees of freedom of such entities.

Reliable BV, or formally analogous, interatomic potentials have been developed for archetypal ferroelectric materials (e.g., $BaTiO_3$, $PbTiO_3$, and $PbZr_{0.2}Ti_{0.8}O_3$) [44–48], hybrid organic-inorganic perovskites (e.g., $MAPbI_3$) [32 and 33] and complex hydrides (e.g., $Li_2B_{12}H_{12}$ and $LiCB_{11}H_{12}$) [49], among others. Recently, the outcomes of molecular dynamics simulations performed with some of those classical force fields have predicted the existence of novel and giant caloric effects [12, 50, and 51].

C. Machine learning potentials

Situations in which the use of first-principles methods is prohibitive and the available classical potentials are not versatile enough to reproduce the phase transition phenomena of interest, machine learning techniques may be very useful. Machine learning (ML) is a subfield of artificial intelligence that exploits the systematic identification of correlation in data sets to make predictions and analysis [52 and 53].

When calculations are performed in a series of similar systems or a number of configurations involving a same system, the results contain redundant information. An example is to run a molecular dynamics simulation in which the total internal energy and atomic forces are calculated at each time step; after a sufficiently long time, points which are close in configurational space and have similar energies are visited during the sampling of the potential-energy surface. Such a redundancy can be exploited to perform computationally intensive calculations (i.e., of first-principles type) only in few selected configurations and then use machine learning (ML) to interpolate between those, thus obtaining approximate solutions for most configurations. The success of this approach depends on a balance between incurred errors due to interpolation and invested computational effort.

ML modeling tools can provide both the energy and atomic forces directly from the atomic positions, hence they can be regarded as a particular class of atomistic potential. ML potentials, however, rely on very flexible analytic functions rather than on physically motivated functionals hence they may be highly versatile without requiring prior detailed knowledge of the simulated system. Promising analytic approaches that have been recently proposed to construct ML potentials include permutation invariant polynomials, the modified Shepard method using Taylor expansions, Gaussian processes and artificial neural networks. Artificial neural networks, in particular, have been demonstrated to be a class of "universal approximators" [54] since allow to approximate unknown multidimensional functions to within arbitrary accuracy for a given set of known function values.

ML potentials are being employed with increasing frequency to solve problems in materials science via atomistic simulations due to their ability to reach high accuracy levels at moderate computational expense (see work [55] for a general review on this topic). In the context of caloric effects, only few works relying on ML techniques can be found in the literature (see, for instance, works [56 and 57]); however, based on the recent progression realized in other similar research fields, we foresee a surge in the application of ML methods to the analysis and prediction of caloric effects in the near future.

III. FREE-ENERGY METHODS

Barocaloric (BC) effects associated with first-order phase transitions that entail abrupt volume and structural changes typically are large. The two main physical descriptors of BC effects are the isothermal entropy change, ΔS_T, and adiabatic temperature change, ΔT_S, associated to the phase transition. These two quantities are thermodynamically related, as we explain next. Consider that the entropy of a condensed matter system depends on temperature and pressure, $S(T, P)$; an infinitesimal entropy variation then can be expressed as:

$$dS = \left(\frac{\partial S}{\partial T} \right)_P dT + \left(\frac{\partial S}{\partial P} \right)_T dP \ . \qquad (12)$$

In an adiabatic process the entropy is conserved, $dS = 0$, thus from the equation above it follows:

$$\frac{C_P}{T} \, dT = - \left(\frac{\partial S}{\partial P} \right)_T dP \ , \qquad (13)$$

in which the constant-pressure heat capacity $C_P \equiv T \left(\partial S / \partial T \right)_P$ has been introduced.

By integrating both sides of the latter equality, one

obtains:

$$\Delta T_S = -\int \frac{T}{C_P}\, dS_T \ . \tag{14}$$

which typically is approximated like [1 and 2]:

$$\Delta T_S \approx -\frac{T_t}{C_P}\cdot \Delta S_T \ , \tag{15}$$

where T_t corresponds to the phase transition temperature and C_P to the averaged heat capacity of the involved phases close to the transition point.

Atomistic simulations generally are performed in the (N,V,T) and (N,P,T) ensembles hence the entropy and other related thermodynamic quantities can be theoretically determined as a function of the state variables V, P, T and ρ ($\equiv N/V$). Concerning BC effects, once the thermodynamic function $S(P,T)$ of the involved phases are known both the ΔS_T and ΔT_S descriptors can be straightforwardly calculated [see Eqs.(12)-(15) above]. Meanwhile, the entropy of a given system is related to its Gibbs free energy, $G(P,T)$, through the expression:

$$S = -\left(\frac{\partial G}{\partial T}\right)_P \ , \tag{16}$$

thus it follows, without too much surprise, that the fundamental quantity allowing for the theoretical determination of BC effects is $G(P,T)$. For this reason, in this section we explain several computational approaches that allow for direct estimation of free energies in crystals by using atomic interaction modeling techniques like those introduced in the previous section (i.e., *ab initio*, classical potential and machine learning methods).

A. The quasi-harmonic approximation

In the quasi-harmonic approach (QHA) [58–60] one assumes that the potential energy of a crystal can be approximated with a quadratic expansion around the equilibrium atomic configuration of the form:

$$E_{\rm qh} = E_{\rm eq} + \frac{1}{2}\sum_{l\kappa\alpha,l'\kappa'\alpha'} \Phi_{l\kappa\alpha,l'\kappa'\alpha'} u_{l\kappa\alpha} u_{l'\kappa'\alpha'} \ , \tag{17}$$

where $E_{\rm eq}$ is the total energy of the equilibrium lattice, $\mathbf{\Phi}$ the corresponding force-constant matrix, and $u_{l\kappa\alpha}$ the displacement along Cartesian direction α of atom κ at lattice site l. The atomic displacements normally are expressed as:

$$u_{l\kappa\alpha}(t) = \sum_q u_{q\kappa\alpha} \exp\left[i\left(\omega t - \boldsymbol{q}\cdot(\boldsymbol{l}+\boldsymbol{\tau}_\kappa)\right)\right] , \tag{18}$$

where $\boldsymbol{q}$ is a wave vector in the first Brillouin zone (BZ) that is defined by the equilibrium unit cell; $\boldsymbol{l}+\boldsymbol{\tau}_\kappa$ is the vector that locates atom κ at cell l in the equilibrium structure. The normal modes of the crystal then are found by diagonalizing the dynamical matrix:

$$D_{\boldsymbol{q};\kappa\alpha,\kappa'\alpha'} = \frac{1}{\sqrt{m_\kappa m_{\kappa'}}}\sum_{l'} \Phi_{0\kappa\alpha,l'\kappa'\alpha'} \exp\left[i\boldsymbol{q}\cdot(\boldsymbol{\tau}_\kappa - \boldsymbol{l'} - \boldsymbol{\tau}_{\kappa'})\right] , \tag{19}$$

and thus the solid can be treated as a collection of non-interacting harmonic oscillators with frequencies $\omega_{\boldsymbol{q}s}$ (positively defined and non-zero) and energy levels:

$$E_{\boldsymbol{q}s} = \hbar\omega_{\boldsymbol{q}s}\left(\frac{1}{2}+n\right) \ , \tag{20}$$

where n is the Bose-Einstein occupation number. Accordingly, the potential energy of a crystal can be written within the QHA like:

$$E_{\rm qh} = \sum_{\boldsymbol{q}s} \hbar\omega_{\boldsymbol{q}s}\left[\frac{1}{2} + \frac{1}{\exp\left(\hbar\omega_{\boldsymbol{q}s}/k_BT\right)-1}\right] \tag{21}$$

and the constant-volume heat capacity like:

$$C_V(T) = \left(\frac{\partial E_{\rm qh}}{\partial T}\right)_V = \sum_{\boldsymbol{q}s} \frac{\left(\hbar\omega_{\boldsymbol{q}s}\right)^2}{k_BT^2}\frac{\exp\left(\hbar\omega_{\boldsymbol{q}s}/k_BT\right)}{\left[\exp\left(\hbar\omega_{\boldsymbol{q}s}/k_BT\right)-1\right]^2} \ . \tag{22}$$

Likewise, the Helmholtz free energy, $F(V,T)$, is analytically expressed as:

$$F(V,T) = E_0(V) + k_BT\sum_{\boldsymbol{q}s}\ln\left[2\sinh\left(\frac{\hbar\omega_{\boldsymbol{q}s}(V)}{2k_{\rm B}T}\right)\right] \ , \tag{23}$$

where E_0 corresponds to the energy of the static lattice and the dependence of the vibrational frequencies on volume has been explicitly noted. The Helmholtz and Gibbs free energies are related through the Legendre transformation $G = F + PV$, in which the pressure is equal to $P = -\left(\partial F/\partial V\right)_T$. Thus, by knowing $F(V,T)$, $C_V(T)$ and the equation of state $P(V,T)$, one can deduce the value of G and C_P as a function of P and T.

Crystals in which anharmonic effects are important (e.g., materials in which imaginary phonon frequencies appear in the vibrational phonon spectra calculated at zero temperature), however, are not adequately described by the QHA (e.g., the Helmholtz free energy expression in Eq.(23) is ill-defined and cannot be evaluated). In such a case, one should resort instead to genuine anharmonic free-energy approaches for the calculation of $F(V,T)$ like molecular dynamics, thermodynamic integration from reference models [42, 43, and 61] and self-consistent phonon approaches [62–65], to cite some examples. The computational load associated with these anharmonic free-energy methods, however, typically is orders of magnitude higher than that of quasi-harmonic approaches. Next, we briefly describe some of them.

B. Molecular dynamics

Molecular dynamics (MD) is a computer simulation method in which the trajectories of atoms in a many-body interacting system are determined numerically by solving the Newton's equations of motion [66 and 67]. For this purpose, one needs to know the forces acting between the particles and their potential energies, which can be calculated by any of the methods described in Sec.II. Thermostat and barostat techniques are employed in MD simulations to render constant temperature and pressure conditions [68]. Temperature and anharmonic effects in materials are naturally accounted for in MD simulations (quantum nuclear effects [58], on the other hand, are systematically disregarded in this approach). Estimation of quantities like T–renormalized phonon frequencies, $\omega(V,T)$, and vibrational density of states, $g(\omega)$, can be obtained from MD simulations by using phonon-mode decomposition [69], force-constant optimization [70] and effective Hamiltonian fitting [71] techniques, to cite some examples.

When the interatomic interactions in MD simulations are described with first-principles methods, typically DFT potentials, they are referred to as *ab initio* molecular dynamics (AIMD). AIMD simulations certainly are several orders of magnitude computationally more intensive than MD simulations performed with classical potentials. Nevertheless, thanks to the current steady growth in computational power and improved algorithms design (e.g., linear scaling DFT methods [72]), reliable AIMD simulation of complex materials currently is within reach (see, for instance, works [73–77]). Machine learning based molecular dynamics, on the other hand, represents an excellent alternative to AIMD simulations (provided that a reliable interaction model can be generated) due to its great balance between numerical accuracy and computational expense [78].

A standard approach to estimate T–renormalized $g(\omega)$'s from MD simulations consists in calculating the Fourier transform of the velocity-velocity autocorrelation function as follows [73–75]:

$$g(\omega) = \frac{1}{N_{ion}} \sum_{i}^{N_{ion}} \int_0^\infty \langle \mathbf{v}_i(t) \cdot \mathbf{v}_i(0) \rangle e^{i\omega t} dt \ , \tag{24}$$

where $\mathbf{v}_i(t)$ represents the velocity of the atom labelled as i at time t, and $\langle \cdots \rangle$ denotes statistical average in the (N,V,T) ensemble. By knowing g(ω), one can easily estimate $F(V,T)$ from the integral expression that is equivalent to Eq.(23), namely:

$$F(V,T) = E_0(V) + \int_0^\infty k_B T \ln \left[2 \sinh \left(\frac{\hbar\omega}{2k_{\rm B}T} \right) \right] g(\omega) d\omega \ . \tag{25}$$

Likewise, the constant-volume heat capacity can be computed by replacing the summation in Eq.(22) with the corresponding integral expression, and the entropy with the formula [79]:

$$S(V,T) = -\left(\frac{\partial F}{\partial T} \right)_V = \int_0^\infty \frac{\hbar\omega}{2T} \coth \left(\frac{\hbar\omega}{2k_{\rm B}T} \right) - k_B \ln \left[2 \sinh \left(\frac{\hbar\omega}{2k_{\rm B}T} \right) \right] g(\omega) d\omega \ . \tag{26}$$

Thus, just like in the QHA method, one can deduce the value of the thermodynamic functions $G(P,T)$ and $C_P(T)$, and in turn of the barocaloric descriptors ΔS_T and ΔT_S, from the knowledge of $F(V,T)$, $C_V(T)$ and $P(V,T)$.

C. Thermodynamic integration

More often than not, accurate estimation of the Helmholtz free energy within an ample thermodynamic interval based on Eqs.(24)–(25) may turn out to be computationally too intensive. In such a situation, thermodynamic integration techniques, in their different variants, may result very useful since they rely on the fact that thermodynamic quantities other than $F(V,T)$ (e.g., the internal energy and pressure) can be numerically converged more efficiently in practice. Two popular modalities of thermodynamic integration (TI) are (1) standard TI and (2) TI from reference models [42, 43, 61, and 80].

Standard TI exploits two well-known thermodynamic relations. First, by considering the hydrostatic pressure expression:

$$\left(\frac{\partial F}{\partial V} \right)_V = -P \ , \tag{27}$$

it is possible to estimate Helmholtz free energy shifts as a function of volume at a fixed temperature like:

$$F(V_1,T) - F(V_0,T) = \int_{V_1}^{V_0} P \ dV \ . \tag{28}$$

Likewise, based on the following expression deduced from statistical mechanics:

$$\left(\frac{\partial \left[\beta F\right]}{\partial \beta} \right)_V = E \ , \tag{29}$$

where $\beta \equiv 1/k_B T$, it is possible to estimate Helmholtz free energy shifts as a function of temperature at a fixed volume like:

$$\beta_1 F(V,T_1) - \beta_0 F(V,T_0) = \int_{\beta_0}^{\beta_1} E \ d\beta \ . \tag{30}$$

In view of Eqs.(28)–(30), it is possible then to extend the value of the Helmholtz free energy by performing MD simulations over a dense grid of (V,T) points, from which P and E can be determined, and subsequently compute the value of the involved integrals numerically.

In the standard TI approach, however, only Helmholtz

free energy differences can be estimated hence for the computation of total free energies of different phases, and therefore of barocaloric effects, the value of $F(V,T)$ should be known at least at one thermodynamic state. TI from a reference model can be very useful for this end. The general principle in this approach is that the change of Helmholtz free energy is computed as the total energy function $E_\lambda(\mathbf{r}_1,\dots\mathbf{r}_N)$ changes adiabatically from E_0 to E_1, the free energies associated with these energy functions being F_0 and F_1. Specifically, the formula for TI from a reference model is [61 and 80]:

$$F_1 - F_0 = \int_0^1 \langle E_1 - E_0 \rangle_\lambda \ , \tag{31}$$

where $\langle\cdots\rangle_\lambda$ represents the thermal average evaluated for the system governed by the energy function $E_\lambda = (1-\lambda)E_0 + \lambda E_1$. In practice, one takes E_1 to be the total energy function whose free energy wish to calculate (e.g., a specific DFT functional), and E_0 the total energy function of a "reference" system whose free energy can be evaluated exactly. For solids, one typically chooses the reference system to be a perfectly harmonic system, the corresponding Helmholtz free energy expression being that in Eqs.(23)–(25). Meanwhile, the integral in Eq. (31) should be computed numerically and for this end one can perform a series of MD simulations in the (N,V,T) ensemble governed by the energy function E_λ at different λ values.

IV. ESTIMATION OF BC EFFECTS

In analogy to the experiments, BC effects can be estimated with atomistic simulations in an indirect, quasi-direct and direct fashion. In the indirect approach, one exploits the Maxwell relation:

$$-\left(\frac{\partial S}{\partial P}\right)_T = \frac{\partial^2 G}{\partial T \partial P} = \left(\frac{\partial V}{\partial T}\right)_P \ , \tag{32}$$

to estimate the adiabatic temperature and isothermal entropy shifts like [see Eq.(13)]:

$$\begin{aligned} \Delta T_S &= \int \frac{T}{C_P}\ \left(\frac{\partial V}{\partial T}\right)_P\ dP \\ \Delta S_T &= -\int \left(\frac{\partial V}{\partial T}\right)_P\ dP \ . \end{aligned} \tag{33}$$

The temperature derivatives in Eq.(33), however, are ill-defined for the case of first-order phase transitions since the volume of the system changes discontinously with temperature during this type of transformation. Accordingly, indirect approaches based on the Maxwell relation above are only valid for estimating BC effects associated with second-order like phase transitions in which the volume of the system changes continuously rather than abruptly [4, 9–11].

As it was mentioned previously, large BC effects typically are associated with first-order phase transitions. In such a case, one can approximately estimate the size of ΔS_T and ΔT_S with the Clausius-Clapeyron method or exactly with quasi-direct and direct techniques. We briefly describe each of these approaches in the following sections.

A. The Clausius-Clapeyron method

To a first approximation, the barocaloric isothermal entropy change associated with a first-order P-induced phase transition can be estimated with the Clausius-Clapeyron relation like [2]:

$$\Delta S_T \approx \Delta S = \Delta V \cdot \frac{dP_t}{dT_t} \ , \tag{34}$$

where ΔV is the volume change that the system experiences during the phase transformation occurring at conditions $P_t(T_t)$ and the derivative is estimated on the corresponding phase boundary line. Meanwhile, the corresponding adiabatic temperature change can be roughly determined with Eq.(15).

The Clausius-Clapeyron (CC) method is not exact and entails few technical problems in practice. First, in experiments the entropy change of the phase transformation, ΔS, is not necessarily equal to the BC descriptor ΔS_T due to the presence of pervasive hysteresis and phase coexistence effects [1], which in general are not reproducible with atomistic simulation techniques (see next Sec.IV B). And second, the value of the derivative and volume change entering Eq.(34) typically are accompanied by large numerical uncertainties that are propagated into the evaluation of ΔS. Having said this, the CC method represents a fair approach to estimate BC effects and it has been already employed in numerous experimental and theoretical works [12, 81, and 82]. In order to estimate BC effects with the highest accuracy, however, it is recommended to employ quasi-direct and direct methods.

B. Quasi-direct estimation of BC effects

The theoretical quasi-direct method emulates the analogous experimental quasi-direct approach (see, for instance, works [3, 83, and 84]) in which essentially the pressure and temperature dependences of the system entropy, $S(P,T)$, are determined (Fig.1). Upon derivation of the full entropy curves (i.e., exhibiting a discontinuity, ΔS, at the first-order phase transition points) obtained at constant pressures P_0 and P_1 and expressed as a function of temperature, it is straightforward to graphically deduce the size of the BC descriptors ΔS_T and ΔT_S on the corresponding S–T diagram, as it is illustrated in Fig.1. From a practical point of view, the

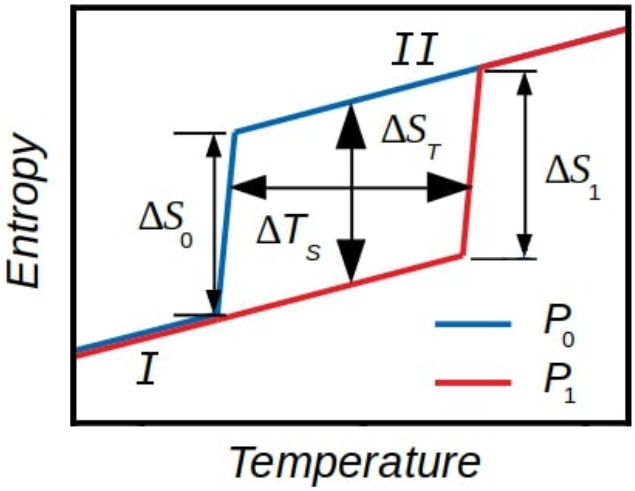

FIG. 1: Sketch of the entropy curves $S(P,T)$ that can be theoretically estimated with computational free-energy methods for a system undergoing a pressure-induced first-order phase transition, $I \rightarrow II$. Hysteresis effects have been disregarded. The BC descriptors ΔS_T and ΔT_S associated with the phase transition can be straightforwardly deduced from these curves. The entropy changes associated with the phase transition, ΔS's, are not necessarily equal to the BC isothermal entropy change ΔS_T.

$S(P,T)$ curves can be calculated numerically with any of the free-energy methods described in Sec.III, and the phase transition points be determined under the condition $G_I(P,T_t) = G_{II}(P,T_t)$ (I and II being the two phases involved in the first-order transformation).

It is worth mentioning, however, that there are important differences between the theoretical and experimental quasi-direct BC approaches. In experiments, the full entropy curves, typically determined with calorimetric techniques, inevitably include hysteresis and phase coexistence effects. Hysteresis, for instance, originates from the fact that in practice transition paths occur under nonequilibrium conditions; consequently, irreversible processes take place within the material. Irreversibility may pose severe limitations to the overall cooling performance attained during successive field-induced cycles, hence it is an important aspect to take into consideration when envisaging possible solid-state cooling applications [85]. Unfortunately, hysteresis, and in general any nonequilibrium process, cannot be reproduced with the simulation techniques reviewed in Sec.III since perfect equilibrium and reversibility conditions are always assumed in them. Thus, in most cases the value of the theoretically estimated BC descriptors should be regarded as upper bounds of the real ΔS_T and ΔT_S shifts (i.e., those measured in the experiments).

C. Direct estimation of BC effects

In this simulation approach, the system is first thermalized at the desired initial temperature and pressure in the (N,P,T), ensemble. After thermalization, the simulation is switched to the isobaric-isoenthalpic ensemble, (N,P,H) [where H represents the enthalpy of the system]. At this stage the hydrostatic pressure is ramped up to the desired final value slowly enough to guarantee adiabaticity, and the accompanying temperature change, $\Delta T_{\rm on}$, is monitored. The system is simulated under these conditions for some time. Subsequently, P is ramped down to its initial value slowly enough again to guarantee adiabaticity and the corresponding temperature change, $\Delta T_{\rm off}$, and final temperature, T_f, are monitored. Under the condition that the system remains in thermal equilibrium during the entire described simulation cycle, it will follow that $T_i = T_f$ and $\Delta T_{\rm on} = \Delta T_{\rm off}$ within the corresponding statistical uncertainties. In such a case, either $\Delta T_{\rm on}$ or $\Delta T_{\rm off}$ can be identified with the adiabatic temperature change associated with the simulated BC process.

The main advantages of using the direct BC simulation method are the little supervision required and possibility to combine pressure with additional external fields (e.g., electric bias) in order to explore original multicaloric effects [1]. The disadvantages, on the other hand, are large computational expense, no direct access to the isothermal entropy change, and the fact that implementation of the (N,P,H) ensemble is rare in most molecular dynamics software packages. To the best of our knowledge, direct estimation of BC effects has been only performed for the hybrid organic-inorganic perovskite $CH_3NH_3PbI_3$ [51], also known as MAPI.

V. REPRESENTATIVE EXAMPLES

In this section, we analyze several illustrative cases in which original BC effects have been simulated and quantified by using atomistic simulation methods. The systems for which those BC effects have been predicted are technologically relevant, namely, fast-ion conductors (LiN_3), orientationally disordered complex hydrides ($Li_2B_{12}H_{12}$) and multiferroic perovskite oxides ($BiFe_{1-x}Co_xO_3$). In these cases, the involved materials modeling techniques comprised molecular dynamics relying on classical force fields (LiN_3 and $Li_2B_{12}H_{12}$) and the quasi-harmonic approximation performed with DFT methods ($BiFe_{1-x}Co_xO_3$). Analogous BC simulation success can be achieved also for other families of pressure responsive materials.

A. Fast-ion conductor LiN_3

Fast-ion conductors (FIC) are materials that exhibit high ionic conductivity in the solid phase [86]. Examples

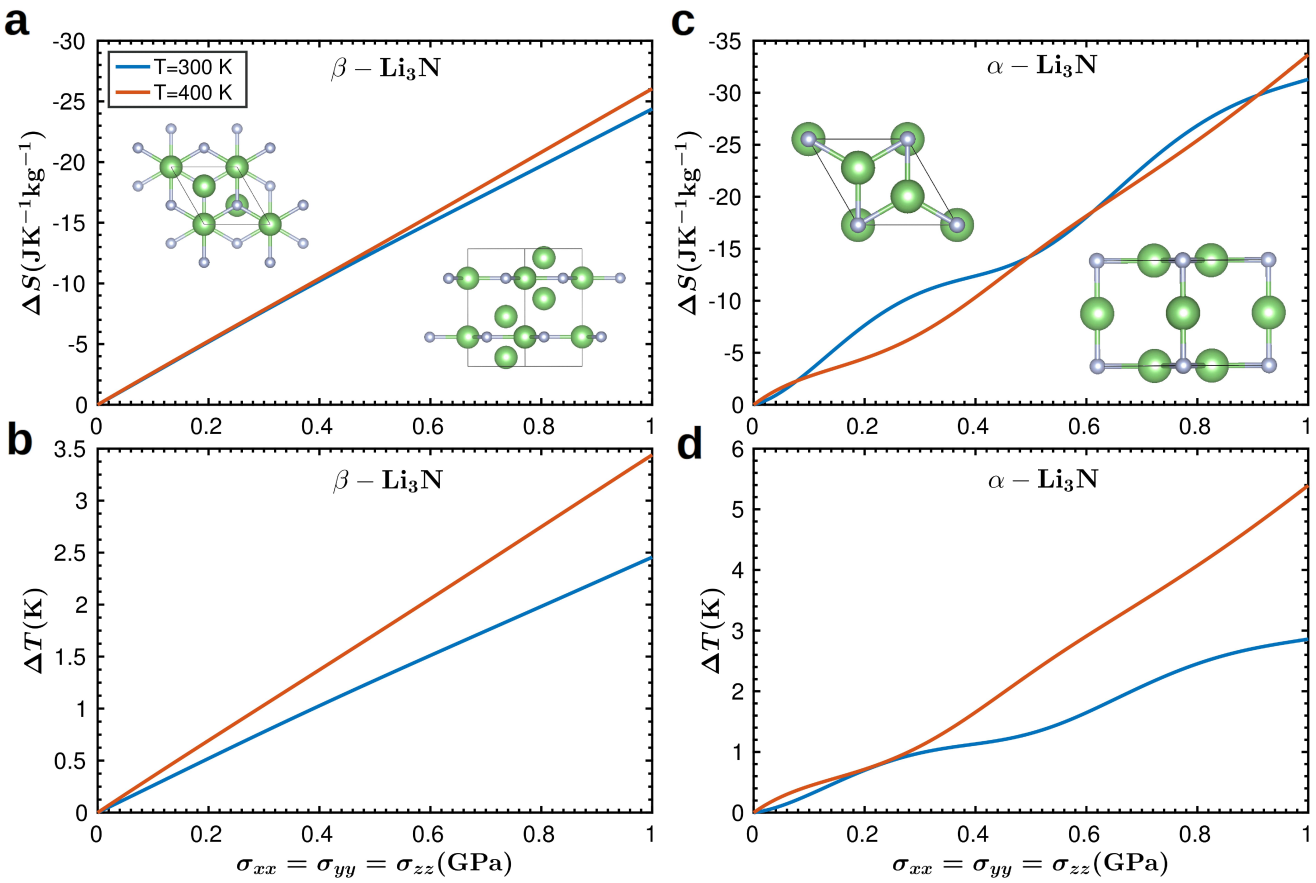

FIG. 2: Predicted barocaloric effects in bulk Li_3N. (a) Isothermal entropy and (b) adiabatic temperature shifts estimated for β-Li_3N. (c) Isothermal entropy and (d) adiabatic temperature shifts estimated for α-Li_3N. Ball-stick representation of the β and α polymorphs of Li_3N; Li and N ions are represented with green and blue spheres, respectively. Adapted from work [10].

of archetypal FIC, also known as *superionic* conductors, include alkali-earth metal fluorides (CaF_2), oxides (doped CeO_2), and lithium-rich compounds ($Li_{10}GeP_2S_{12}$). Inherent to superionicity is a significant increase in the concentration of point defects (e.g., Frenkel pair defects) associated to a particular sublattice of atoms in the crystal. Due to their unique ion-transport properties, FIC are promising materials for the realization of all-solid-state electrochemical batteries via replacement of customary liquid electrolytes, which involves substantial improvements with respect to standard batteries in terms of safety, cyclability, and electrochemical performance [87]. Owing to the large entropy change (typically of the order of 100 J K^{-1} [86]) and external tunability associated with the superionic phase transition [34, 88, and 89], FIC also are being established as auspicious caloric materials for exploitation in solid-state cooling applications [3, 4, 10, 11, and 90].

Figure 2 shows the two common polymorphs of bulk Li_3N, a structurally simple and well-known lithium-based FIC. The α phase (hexagonal, space group $P6/mmm$) has a layered structure composed of alternating planes of hexagonal Li_2N and pure Li^+ ions. The β phase (hexagonal, space group $P6_3/mmmc$) presents an additional layer of lithium ions intercalated between the Li_2N planes that is accompanied by a doubling of the unit cell. Exceptionally high ionic conductivities of the order of 10^{-4}–10^{-3} S cm^{-1} have been experimentally observed in Li_3N at room temperature [91–93]. In molecular dynamics simulation studies based on classical interaction potentials and first-principles methods [10], it has been found that in order to reproduce room-temperature superionicity in β–Li_3N it is necessary to introduce a small concentration of extrinsic Li^+ vacancies in the system ($\sim 1\%$); by contrast, stoichiometric α–Li_3N already displays fast-ionic conductivity at $T = 300$ K.

Figure 2 also encloses the theoretical estimation of BC effects in Li_3N up to 1 GPa at room temperature and $T = 400$ K [10]. Those calculations relied on molecular dynamics simulations performed with classical interatomic potentials (Sec.II B) and the set of equations Eq.(33). In the β phase, a maximum room-temperature entropy shift of -24 $\mathrm{JK^{-1}kg^{-1}}$ was obtained, which slightly increases in absolute value at higher temperatures (Fig.2a).

The magnitude of such ΔS can be regarded as "giant" (i.e., $|\Delta S| > 10$ JK^{-1}kg^{-1}). The accompanying adiabatic temperature shifts, however, are large but not giant (that is, $|\Delta T| < 10$ K, Fig.2b) owing to the huge heat capacity of Li_3N (e.g., $\sim 4 \cdot 10^3$ JK^{-1}kg^{-1} at $T = 300$ K). Analogous BC results were found in α–Li_3N (Figs.2c–d) although in this latter case the estimated isothermal entropy and adabatic temperature changes were slightly larger (for instance, $\Delta S = -32$ JK^{-1}kg^{-1} and $\Delta T = +2.8$ K at $T = 300$ K and $\sigma = 1$ GPa).

The large BC effects found in superionic Li_3N are not driven by any structural phase transformation. This assertion is confirmed, for instance, by the radial distribution functions calculated for all pairs of ionic species in Li_3N at $T = 300$ K since they present almost identical structural traits independently of the applied pressure [10]. Such an absence of phase transformation is in stark contrast to what is observed in other BC materials in which most of the caloric response is concentrated near phase transition points [2]. Then, which is the principal mechanism behind the disclosed giant ΔS in Li_3N? It is well-known that hydrostatic pressure depletes significantly ionic diffusivity, and therefore the entropy, in most fast-ion conductors [34, 86, 88, and 89]. Essentially, the available volume to interstitial ions is effectively reduced under compression and as a consequence the kinetic barriers and formation energy of defects governing ion migration drastically increase. Thus, increasing compression steadily depletes ionic diffusion and in turn the entropy of the FIC crystal.

Therefore, in work [10] and original and rational strategy for achieving large (and possibly also reversible) BC effects at ambient temperature based on fast-ion conductors was introduced and illustrated for bulk Li_3N. Instead of focusing on the triggering of a structural phase transition, which only serendipitously will occur at room temperature, the starting point in this new scenario is a material that is already superionic at ambient conditions. Large BC effects then can be obtained trough the application of hydrostatic pressure since this affects significantly and sustainedly the ionic conductivity, and in turn the entropy and volume, of fast-ion conductors.

B. Complex hydride $Li_2B_{12}H_{12}$

Recently, colossal barocaloric effects (defined as $|\Delta S| \sim 100$ JK^{-1}kg^{-1}) have been measured in two different families of materials that display intriguing order-disorder phase transitions [3, 81, and 83]. First, giant barocaloric effects have been theoretically predicted [9] and experimentally observed in the archetypal superionic compound AgI [3]. AgI exhibits a first-order normal (low-entropy) to superionic (high-entropy) phase transition that responds to both temperature and pressure and which involves the presence of highly mobile silver ions in the high–T superionic state [86]. Likewise, the entropy changes estimated for other similar superionic phase transitions in general are also large [4, 10, and 11]. And second, colossal barocaloric effects have been reported for the molecular solid neopentylglycol [81 and 83], $(CH_3)_2C(CH_2OH)_2$, and other plastic crystals [84]. In these solids, molecules reorient almost freely around their centers of mass, which remain localized at well-defined lattice positions. Molecular rotations lead to orientational disorder, which renders high entropy. By using hydrostatic pressure, it is possible to block such molecular reorientational motion and thus induce a fully ordered state characterized by low entropy [94]. The barocaloric effects resulting from this class of first-order order-disorder phase transition are huge and comparable in magnitude to those achieved in conventional refrigerators with environmentally harmful gases [81, 83, and 84].

In work [12], it has been predicted the occurrence of colossal barocaloric effects ($|\Delta S| \sim 100$ JK^{-1}kg^{-1}) in the energy material $Li_2B_{12}H_{12}$ (LBH), a complex hydride that is already known from the fields of hydrogen storage [95–97] and solid-state batteries [98 and 99]. By using molecular dynamics simulations [100], a pressure-induced isothermal entropy change of $|\Delta S| = 367$ JK^{-1}kg^{-1} and an adiabatic temperature change of $|\Delta T| = 43$ K at $T = 480$ K have been identified. These colossal entropy and temperature changes were driven by small hydrostatic pressure shifts of ~ 0.1 GPa (Fig.3), thus yielding gigantic barocaloric strengths of $|\Delta S|/P \sim 10^3$ JK^{-1}kg^{-1}GPa^{-1} and $|\Delta T|/P \sim 10^2$ K GPa^{-1}. The colossal barocaloric effects disclosed in bulk LBH are originated by simultaneous frustration of Li^+ diffusion and $(BH)_{12}^{-2}$ icosahedra reorientational motion driven by hydrostatic pressure.

Specifically, at ambient conditions lithium dodecahydrododecaborate ($Li_2B_{12}H_{12}$), LBH, presents an ordered cubic $Pa\bar{3}$ phase ($Z = 4$), referred to as α, which is characterized by Li^+ cations residing on near-trigonal-planar sites surrounded by three $(BH)_{12}^{-2}$ icosahedron anions. In turn, each $(BH)_{12}^{-2}$ anion resides in an octahedral cage surrounded by six Li^+ cations (Fig.3a). A symmetry preserving order-disorder phase transition occurs at high temperatures (~ 600 K) that stabilises a disordered state, referred to as β, in which the Li^+ cations are mobile and the $(BH)_{12}^{-2}$ anions present reorientational motion (Fig.3a). The relative volume expansion that has been experimentally measured for such a first-order order-disorder phase transition is $\Delta V^{\text{expt}}/V_\alpha^{\text{expt}} \approx 8\%$ [98] and the corresponding phase transition enthalpy $\Delta H^{\text{expt}} \approx 130$ kJ kg^{-1} [101]. The huge volume variation and enthalpy associated with the $\alpha \leftrightarrow \beta$ transformation could be propitious for barocaloric purposes if the involved phase transition was responsive to small hydrostatic pressure shifts of ~ 0.1 GPa.

Figure 3b shows the P–T phase diagram of bulk LBH theoretically estimated with MD techniques [100]. The coexistence line of the α and β phases was determined by conducting numerous MD simulations at small P–T shifts of 0.05 GPa and 12.5 K, and by monitoring the structural, Li^+ diffusion, and $(BH)_{12}^{-2}$ reorientational

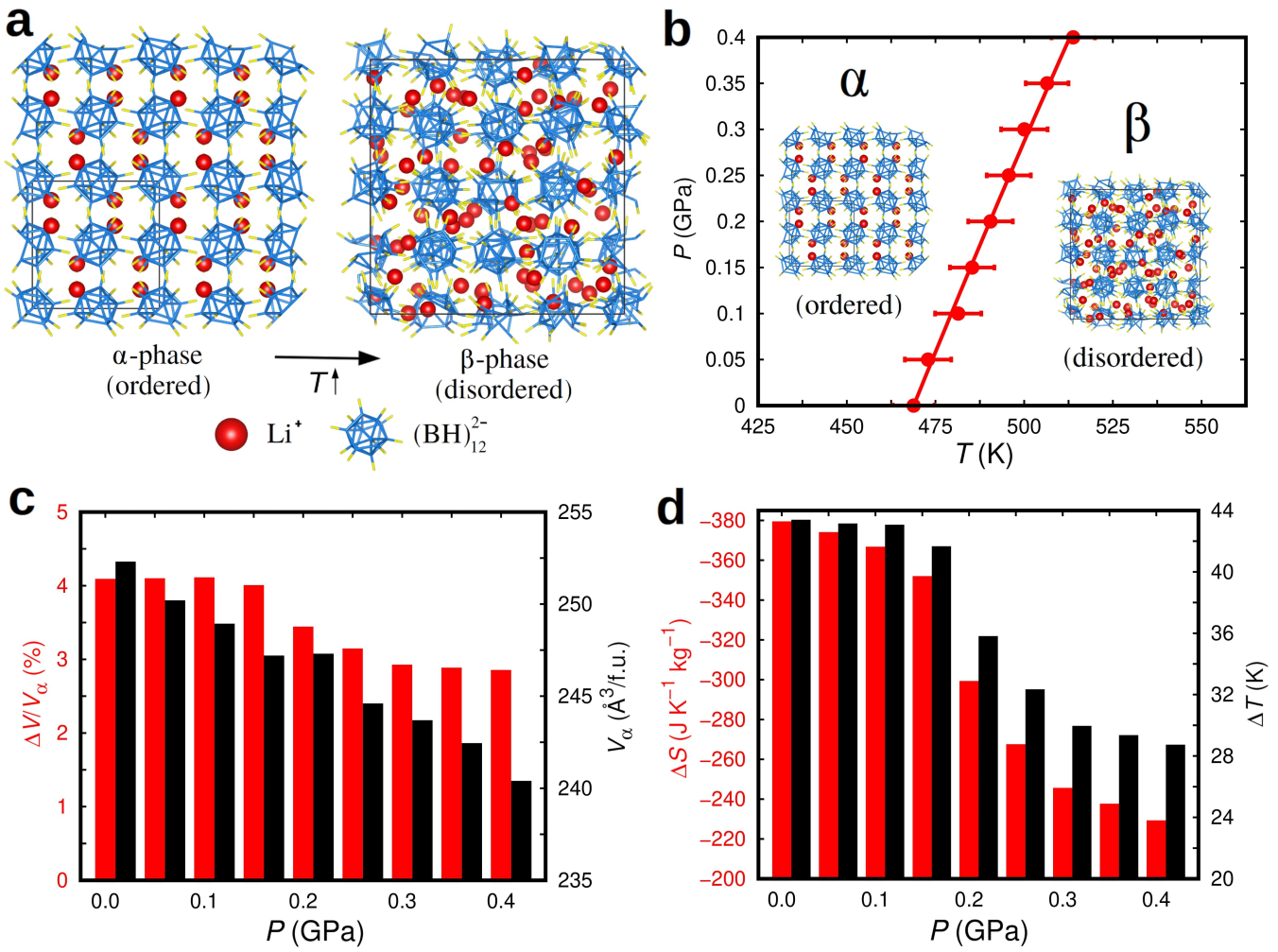

FIG. 3: (a) Low-T (ordered) and high-T (disordered) phases of bulk $Li_2B_{12}H_{12}$. Li, B, and H ions are represented with red, blue, and yellow colours, respectively. (b) Estimated $Li_2B_{12}H_{12}$ phase diagram expressed as a function of pressure and temperature. (c) Relative volume change associated with the T-induced $\alpha \rightarrow \beta$ phase transition expressed as a function of pressure (red); volume of the α phase per formula unit (f.u.), V_α, at the phase-transition conditions (black). (d) Isothermal entropy (red) and adiabatic temperature (black) changes associated with the barocaloric response of bulk $Li_2B_{12}H_{12}$ expressed as a function of pressure. Adapted from work [12].

properties of the system. In consistency with the experiments, a point in the α–β coexistence line of Fig.3b was identified with sharp and simultaneous changes in the volume (Fig.3c), Li^+ diffusion coefficient (D_{Li}), and $(BH)_{12}^{2-}$ reorientational frequency ($\lambda_{B_{12}H_{12}}$) of bulk LBH. It was found that the critical temperature of the $\alpha \leftrightarrow \beta$ transformation can be certainly displaced by hydrostatic pressure (i.e., roughly by 13 K per 0.1 GPa).

Consequently, the BC isothermal entropy and adiabatic temperature shifts induced by pressures of $0 \leq P \leq 0.4$ GPa in bulk LBH were theoretically estimated in work [12]. For this end, and in view of the first-order nature of the $\alpha \leftrightarrow \beta$ phase transformation [98], the Clausius-Clapeyron method was employed (Sec.IV A). The resulting ΔS and ΔT values enclosed in Fig. 3d in fact render colossal barocaloric effects. For example, at $T = 480$ K and $P = 0.1$ GPa an isothermal entropy change of -367 $JK^{-1}kg^{-1}$ and an adiabatic temperature change of $+43$ K were estimated. The size of ΔS and ΔT were found to gradually decrease under pressure (e.g., at $T = 515$ K and $P = 0.4$ GPa we estimated -229 $JK^{-1}kg^{-1}$ and $+28$ K, respectively). Meanwhile, the predicted LBH barocaloric effects were always direct, that is, $\Delta T > 0$, since the low-entropy ordered phase (α) was stabilized over the high-entropy disordered phase (β) under pressure ($\Delta S < 0$).

The phase transition underlying the colossal barocaloric effects enclosed in Fig.3 is quite remarkable since it combines key ingredients of fast-ion conductors (i.e., ionic diffusion) and molecular crystals (i.e., reorientational motion), materials that individually have been proven to be excellent BC materials. Thus, alkali-metal

complex borohydrides ($A_2B_{12}H_{12}$, A = Li, Na, K, Cs [102 and 103]) emerge as a promising new family of caloric materials in which the salient phase-transition features of fast-ion conductors and plastic crystals coexist and cooperate to render colossal barocaloric effects, broadening so the range of caloric materials with commercial potential for solid-state cooling applications.

C. Supertetragonal oxide perovskite $BiFe_{1-x}Co_xO_3$

Super-tetragonal ($\mathcal{T}$) oxide perovskites comprise a family of materials that are fundamentally intriguing and have great potential for ferroelectric, piezoelectric, sensor, and energy conversion applications [104–106]. Supertetragonal phases exhibit giant electric polarizations of the order of 100 μC/cm^2 and may be accompanied by magnetism. The coexistence of ferroelectricity and magnetism in crystals, known as multiferroics, offers the possibility of controlling the magnetization with electric fields via their cross-order coupling. Magnetoelectric couplings can be used, for example, to design ultra efficient logic and memory devices and realize large piezomagnetic coefficients for the miniaturization of antennas and sensors. Furthermore, phase transitions involving $\mathcal{T}$ phases typically exhibit colossal volume changes of $\sim 10\%$ (e.g., $PbVO_3$ and related solid solutions), which can be exploited in mechanical degradation [107 and 108] applications. Examples of $\mathcal{T}$ multiferroic materials are bulk $BiCoO_3$ (BCO) and $BiFeO_3$ (BFO) thin films [13, 109, and 110].

Recently, it has been shown by means of first-principles calculations based on DFT that $BiFe_{1-x}Co_xO_3$ solid solutions (BFCO) with $0.25 \leq x \leq 0.50$ represent ideal bulk systems in which to realize the full potential of multiferroic $\mathcal{T}$ materials [111]. Specifically, it has been found that under moderate hydrostatic pressures of $0.1 \lesssim P \lesssim 1$ GPa (depending on the relative Fe/Co content) it is possible to trigger a phase transition from a low-T rhombohedral ($\mathcal{R}$) phase to a high-T $\mathcal{T}$ phase (Figs.4a–c) at room temperature. The disclosed pressure-induced $\mathcal{R} \rightarrow \mathcal{T}$ phase transformation involves (i) a colossal increase in the electric polarization of $\sim 150\%$, (ii) the existence of a robust net magnetization of ≈ 0.13 μ_B per formula unit, and (iii) a giant volume increase of $\Delta V \sim 10\%$ (Fig.4d). Examples of technologies in which these multifunctional phenomena could have an impact include pyroelectric energy harvesting [112 and 113] and solid-state cooling [114].

Figures 4d and e show respectively the isothermal entropy and adiabatic temperature changes induced by hydrostatic pressure in $BiFe_{0.5}Co_{0.5}O_3$ solid solutions. Those results have been obtained with the quasi-harmonic DFT method (Sec.III A) and the Clausius-Clapeyron indirect estimation approach (Sec.IV A) [115]. First, it is noted that the $\mathcal{R} \rightarrow \mathcal{T}$ transition temperature can be enormously shifted by small pressure changes (Fig.4c). For instance, in $BiFe_{0.5}Co_{0.5}O_3$ a compression decrease of only 0.06 GPa moves the transition temperature from room temperature down to about 200 K. Second, an isothermal entropy change of approximately -1.5 J K^{-1}mol^{-1} (equivalent to ≈ -4.8 J K^{-1}kg^{-1}) is estimated at room temperature along with a ΔT of ≈ 5 K. These figures, although cannot be regarded as "giant", are reasonably large and promising. And third, the size of these two barocaloric descriptors significantly increase at lower temperatures. At $T = 200$ K, for instance, ΔS increases up to -2.8 J K^{-1}mol^{-1} and ΔT to 6.6 K.

The driving pressures reported in Fig.4d are very large, of the order of 1 GPa; however, in practice those values can be drastically reduced (i.e., by one order of magnitude, ~ 0.1 GPa) by increasing the relative content of Fe ions. For instance, by using analogous first-principles computational methods a $\mathcal{R} \rightarrow \mathcal{T}$ phase transition pressure of 0.2 GPa is estimated at zero temperature for bulk $BiFe_{0.75}Co_{0.25}O_3$ [115]. This theoretical outcome is in good agreement with the available experimental data on the compositional phase diagram of BFCO solid solutions [116]. Another interesting aspect of BFCO solid solutions is that, besides hydrostatic pressure, they can react to external magnetic and electric fields since these are simultaneously magnetic and ferroelectric [111]. Such a multifunctional quality converts BFCO solid solutions into a potentially ideal playground in which to explore and take advantage of novel multicaloric effects and cycles [1 and 114]. Therefore, BFCO solid solutions in particular and multiferroic materials exhibiting supertetragonal phases in general, appear to be very promising materials for the development of advanced solid-state cooling applications.

VI. CONCLUSIONS

Atomistic computational techniques for the simulation of barocaloric effects are already well established. The simulation methods reviewed in this Chapter (e.g., quasi-harmonic and thermodynamic integration techniques) were originally developed for the study of temperature- and pressure-induced phase transformations in materials, and have already achieved great success in many research disciplines (e.g., high-pressure physics). Nonetheless, the number of atomistic simulation studies found in the literature on barocaloric effects currently is quite reduced and mostly limited to indirect estimation approaches. One of the main objectives of this Chapter is to improve this situation by surveying key theoretical and computational concepts in the estimation of barocaloric effects and to promote the use of alternative and highly accurate direct and quasi-direct simulation methods.

As it has been illustrated here, atomistic simulation approaches can be used to reproduce with reliability the barocaloric performance of complex materials like multiferroics, in which the structural and electronic degrees of freedom are strongly coupled, lithium-based hydrides, in which molecular ions can be orientationally disor-

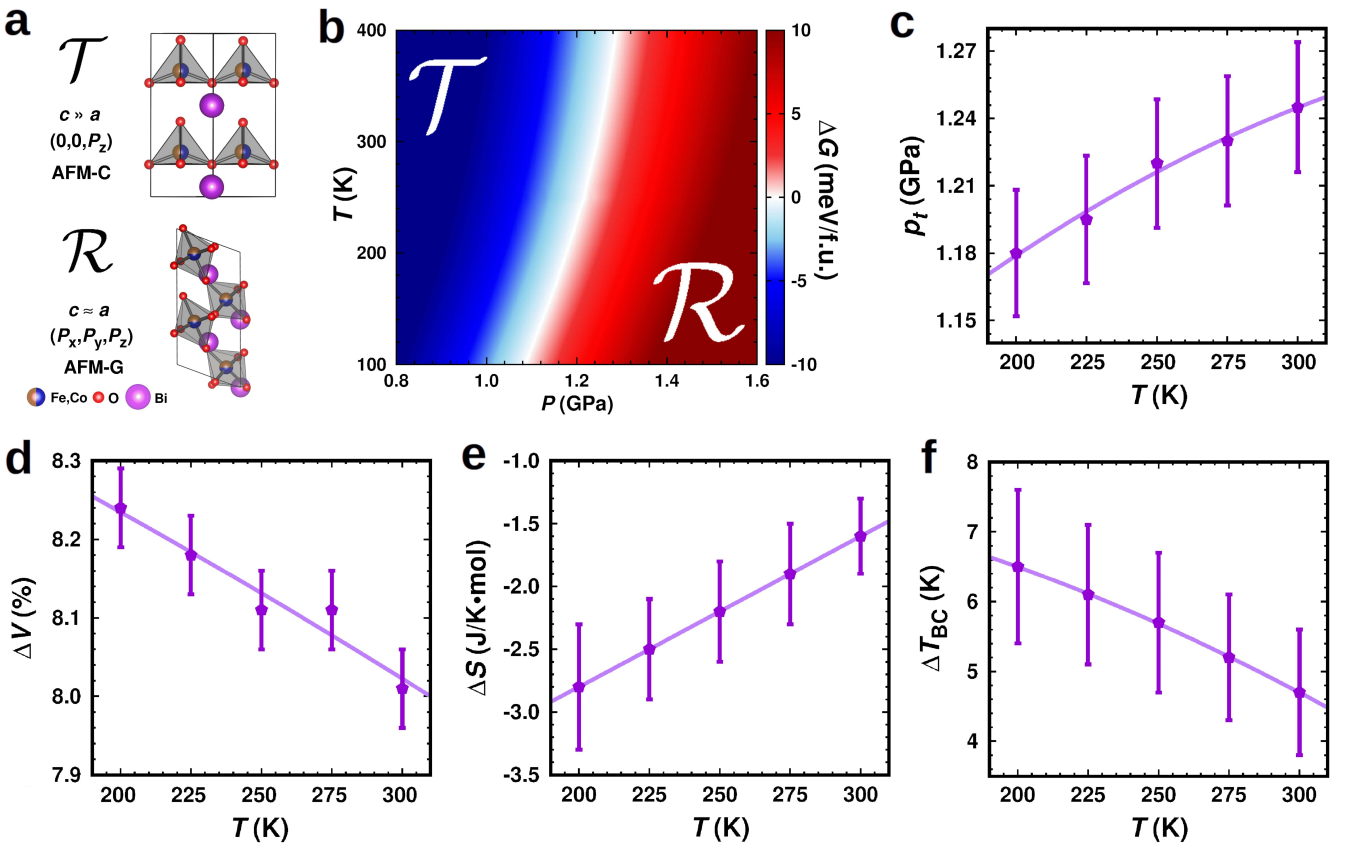

FIG. 4: (a) Description of the two energetically competing structures in bulk BFCO under pressure. (b) Gibbs free energy difference between the $\mathcal{T}$ and $\mathcal{R}$ phases of bulk BFCO expressed as a function of pressure and temperature. (c) Phase boundary delimiting the stability region of the $\mathcal{T}$ and $\mathcal{R}$ phases of bulk BFCO. (d) Relative volume change occurring during the pressure-induced $\mathcal{T} \rightarrow \mathcal{R}$ phase transition and expressed as a function of temperature. (e) Isothermal entropy and (f) adiabatic temperature changes estimated for the pressure-induced $\mathcal{T} \rightarrow \mathcal{R}$ phase transition expressed as a function of temperature.

dered, and fast-ion conductors, in which ionic diffusion determines most of their physical properties. Analogous barocaloric simulation success can be achieved for other families of functional materials exhibiting complex and unconventional, as well as standard, responses to hydrostatic pressure.

Atomistic simulation of barocaloric effects, therefore, can indeed help enormously in developing new materials and strategies for boosting solid-state cooling based on the application of hydrostatic pressure. Thus, the current pressing challenge of finding new refrigeration technologies that are environmentally friendly and also sustainable may greatly benefit from the reliable and physically insightful computational methods surveyed in this Chapter.

[1] Cazorla, C., Novel mechanocaloric materials for solid-state cooling applications, Appl. Phys. Rev. **6**, 041316 (2019).

[2] Moya, X., Kar-Narayan, S. & Mathur, N. D., Caloric materials near ferroic phase transitions, Nat. Mater. **13**, 439 (2014).

[3] Aznar, A., Lloveras, P., Romanini, M., Barrio, M., Tamarit, J. Ll., Cazorla, C., Errandonea, D., Mathur, N. D., Planes, A., Moya, X. & Mañosa, Ll., Giant barocaloric effects over a wide temperature range in superionic conductor AgI, Nat. Commun. **8**, 1851 (2017).

[4] Cazorla, C & Errandonea, D., Giant mechanocaloric effects in fluorite-Structured superionic materials, Nano Lett. **16**, 3124 (2016).

[5] Scott, J. F., Electrocaloric materials, Annu. Rev. Mater. Res. **41**, 229 (2011).

[6] Pecharsky, V. K. & Gschneidner, Jr. K. A., Giant magnetocaloric effect in $Gd_5(Si_2Ge_2)$, Phys. Rev. Lett. **78**, 4494 (1997).

[7] Bonnot, E., Romero, R., Mañosa, Ll., Vives, E. &

Planes, A., Elastocaloric effect associated with the martensitic transition in shape-memory alloys, Phys. Rev. Lett. **100**, 125901 (2008).

[8] Shirsath, S. E. *et al.*, Interface-charge induced giant electrocaloric effect in lead free rerroelectric thin-film bilayers, Nano Lett. **20**, 1262 (2020).

[9] Sagotra, A. K., Errandonea, D. & Cazorla, C., Mechanocaloric effects in superionic thin films from atomistic simulations, Nat. Commun. **8**, 963 (2017).

[10] Sagotra, A. K., Chu, D. & Cazorla, C., Room-temperature mechanocaloric effects in lithium-based superionic materials, Nat. Commun. **9**, 3337 (2018).

[11] Min, J., Sagotra, A. K. & Cazorla, C., Large barocaloric effects in thermoelectric superionic materials, Phys. Rev. Mater. **4**, 015403 (2020).

[12] Sau, K., Ikeshoji, T., Takagi, S., Orimo, S.-I., Errandonea, D., Chu, D. & Cazorla, C., Colossal barocaloric effects in the complex hydride $Li_2B_{12}H_{12}$, Sci. Rep. **11**, 11915 (2021).

[13] Menéndez, C., Chu, D. & Cazorla, C., Oxygen-vacancy induced magnetic phase transitions in multiferroic thin films, npj Comput. Mater. **6**, 76 (2020)

[14] Machado, P. *et al.*, Enhancement of phase stability and optoelectronic performance of $BiFeO_3$ thin films via cation co-substitution, J. Mater. Chem. C **9**, 330 (2021).

[15] Kohn, W. & Sham, L. J., Self-consistent equations including exchange and correlation effects, Phys. Rev. **140**, A1133 (1965).

[16] Sham, L. J. & Kohn, W., One-particle properties of an inhomogeneous interacting electron gas, Phys. Rev. **145**, 561 (1966).

[17] Ceperley, D. M. & Alder, B. J., Ground state of the electron gas by a stochastic method, Phys. Rev. Lett. **45**, 566 (1980).

[18] Perdew, J. P. & Zunger, A., Self-interaction correction to density-functional approximations for many-electron systems, Phys. Rev. B **23**, 5048 (1981).

[19] Perdew, J. P., J. A. Chevary, S. H. Vosko, K. A. Jackson, M. R. Pederson, D. J. Singh & Fiolhais, C., Atoms, molecules, solids, and surfaces: Applications of the generalized gradient approximation for exchange and correlation, Phys. Rev. B **46**, 6671 (1992).

[20] Perdew, J. P., K. Burke & Ernzerhof, M., Generalized gradient approximation made simple, Phys. Rev. Lett. **77**, 3865 (1996).

[21] Sun, J., Ruzsinszky, A. & Perdew, J. P., Strongly constrained and appropriately normed semilocal density functional, Phys. Rev. Lett. **115**, 036402 (2015).

[22] Zhang, Y. *et al.*, Efficient first-principles prediction of solid stability: Towards chemical accuracy, npj Comp. Mater. **4**, 9 (2018).

[23] Becke, A. D., Density-functional thermochemistry. III. The role of exact exchange, J. Chem. Phys. **98**, 5648 (1993).

[24] Adamo, C. & Barone, V., Toward reliable density functional methods without adjustable parameters: The PBE0 model, J. Chem. Phys. **110**, 6158 (1999).

[25] Krukau, A. V., Vydrov, O. A., Izmaylov, A. F. & Scuseria, G. E., Influence of the exchange screening parameter on the performance of screened hybrid functionals, J. Chem. Phys. **125**, 224106 (2006).

[26] Franchini, C., Hybrid functionals applied to perovskites, J. Phys. Condens. Matt. **26**, 253202 (2014).

[27] Bilc, D. I., Orlando, R., Shaltaf, R., Rignanese, G.-M., Íñiguez, J. & Ghosez, Ph., Hybrid exchange-correlation functional for accurate prediction of the electronic and structural properties of ferroelectric oxides, Phys. Rev. B **77**, 165107 (2008).

[28] Rivero, P. & Cazorla, C., Revisiting the zero-temperature phase diagram of stoichiometric $SrCoO_3$ with first-principles methods, Phys. Chem. Chem. Phys. **18**, 30686 (2016).

[29] Cazorla, C., Lattice effects on the formation of oxygen vacancies in perovskite thin films, Phys. Rev. Appl. **7**, 044025 (2017).

[30] Ercolessi, F. & Adams, J. B., Interatomic potentials from first-principles calculations: The force-matching method, Europhys. Lett. **26**, 583 (1994).

[31] Cazorla, C. & Boronat, J., First-principles modeling of three-body interactions in highly compressed solid helium, Phys. Rev. B **92**, 224113 (2015).

[32] Mattoni, A., Filipetti, A., Saba, M. I. & Delugas, P., Methylammonium rotational dynamics in lead halide perovskite by classical molecular dynamics: The role of temperature, J. Phys. Chem. C **119**, 17421 (2015).

[33] Hata, T., Giorgi, G., Yamashita, K., Caddeo, C. & Mattoni, A., Development of a Classical Interatomic Potential for $MAPbBr_3$, J. Phys. Chem. C **121**, 3724 (2017).

[34] Cazorla, C., Sagotra, A. K., King, M. & Errandonea, D., High-pressure phase diagram and superionicity of alkaline earth metal difluorides, J. Phys. Chem. C **122**, 1267 (2018).

[35] Tinte, S., Stachiotti, M. G., Sepliarsky, M., Migoni, R. L. & Rodriguez, C. O., Atomistic modelling of $BaTiO_3$ based on first-principles calculations, J. Phys.:Condens. Matt. **11**, 9679 (1999).

[36] Jackson, R. A. & Valerio, M. E. G., Structural phase transition and dynamical properties of $PbTiO_3$ simulated by molecular dynamics, J. Phys.:Condens. Matt. **17**, 837 (2005).

[37] Sepliarsky, M., Phillpot, S. R., Wolf, D., Stachiotti, M. G. & Migoni, R. L., Ferroelectric properties of $KNbO_3/KTaO_3$ superlattices by atomic-level simulation, J. Appl. Phys. **90**, 4509 (2001).

[38] Hashimoto, T. & Moriwake, H., Dielectric properties of $BaTiO_3$ by molecular dynamics simulations using a shell model, Mol. Simul. **41**, 1074 (2015).

[39] Gambuzzi, E. & Pedone, A., On the structure of Ce-containing silicophosphate glasses: a core-shell molecular dynamics investigation, Phys. Chem. Chem. Phys. **16**, 21645 (2014).

[40] Cohen, R. E., Origin of ferroelectricity in perovskite oxides, Nature **358**, 136 (1992).

[41] Haomin, C. & Adams, S., Bond softness sensitive bond-valence parameters for crystal structure plausibility tests, IUCrJ **4**, 614 (2017).

[42] Taioli, S., Cazorla, C., Gillan, M. J. & Alfè, D., Melting curve of tantalum from first principles, Phys. Rev. B **75**, 214103 (2007).

[43] Cazorla, C., Gillan, M. J., Taioli, S. & Alfè, D., Ab initio melting curve of molybdenum by the phase coexistence method, J. Chem. Phys. **126**, 194502 (2007).

[44] Grinberg, I., Cooper, V. R. & Rappe, A. M., Relationship between local structure and phase transitions of a disordered solid solution, Nature **419**, 909 (2002).

[45] Grinberg, I., Cooper, V. R. & Rappe, A. M., Oxide chemistry and local structure of $PbZr_xTi_{1-x}O_3$ studied by density-functional theory supercell calculations,

Phys. Rev. B **69**, 144118 (2004).
[46] Shin, Y.-H., Cooper, V. R., Grinberg, I. & Rappe, A. M., Development of a bond-valence molecular-dynamics model for complex oxides, Phys. Rev. B **71**, 054104 (2005).
[47] Liu, S., Grinberg, I., Takenaka, H. & Rappe, A. M., Reinterpretation of the bond-valence model with bond-order formalism: An improved bond-valence-based interatomic potential for $PbTiO_3$, Phys. Rev. B **88**, 104102 (2013).
[48] Xu, R., Liu, S., Grinberg, I., Karthik, J., Damodaran, A. R., Rappe, A. M. & Martin, L. W., Ferroelectric polarization reversal via successive ferroelastic transitions, Nat. Mater. **14**, 79 (2015).
[49] Sau, K., Ikeshoji, T., Kim, S., Takagi, S. & Orimo, S.-I. Comparative molecular dynamics study of the roles of anion–cation and cation–cation correlation in cation diffusion in $Li_2B_{12}H_{12}$ and $LiCB_{11}H_{12}$, Chem. Mater. **33**, 2357 (2021).
[50] Qi, Y., Liu, S., Lindenberg, A. M. & Rappe, A. M., Ultrafast electric field pulse control of giant temperature change in ferroelectrics, Phys. Rev. Lett. **120**, 055901 (2015).
[51] Liu, S. & Cohen, R. E., Response of methylammonium lead iodide to external stimuli and caloric effects from molecular dynamics simulations, J. Phys. Chem. C **120**, 17274 (2016).
[52] Behler, J., Neural network potential-energy surfaces for atomistic simulations, Chem. Modell. **7**, 1 (2010).
[53] Rupp, M., Machine learning for quantum mechanics in a nutshell, Int. J. Quantum Chem. **115**, 1058 (2015).
[54] Behler, J., Constructing high-dimensional neural network potentials: A tutorial review, Int. J. Quantum Chem. **115**, 1032 (2015).
[55] Deringer, V. L., Caro, M. A. & Csanyi, G. Machine learning interatomic potentials as emerging tools for materials science, Adv. Mater. **31**, 1902765 (2019).
[56] Zhang, Y. & Xu, X. Machine learning the magnetocaloric effect in manganites from compositions and structural parameters, AIP Adv. **10**, 035220 (2020).
[57] Gong, J., Chu, S., Mehta, R. K. & McGaughey, A. J. H. XGBoost model for electrocaloric temperature change prediction in ceramics, npj Comput. Mater. **8**, 140 (2022).
[58] Cazorla, C. & Boronat, J., Simulation and understanding of atomic and molecular quantum crystals, Rev. Mod. Phys. **89**, 035003 (2017).
[59] Baroni, S., Giannozzi, P. & Isaev, E., Density-functional perturbation theory for quasi-harmonic calculations, Rev. Mineral. Geochem. **71**, 39 (2010).
[60] Cazorla, C., Errandonea, D. & Sola, E., High-pressure phases, vibrational properties, and electronic structure of $Ne(He)_2$ and $Ar(He)_2$: A first-principles study, Phys. Rev. B **80**, 064105 (2009).
[61] Cazorla, C., & Alfè, D. & Gillan, M. J., Constraints on the phase diagram of molybdenum from first-principles free-energy calculations, Phys. Rev. B **85**, 064113 (2012).
[62] Tadano, T. & Tsuneyuki, S., Self-consistent phonon calculations of lattice dynamical properties in cubic $SrTiO_3$ with first-principles anharmonic force constants, Phys. Rev. B **92**, 054301 (2015).
[63] Souvatzis, P., Eriksson, O., Katsnelson, M. I. & Rudin, S. P., Entropy driven stabilization of energetically unstable crystal structures explained from first principles theory, Phys. Rev. Lett. **100**, 095901 (2008).
[64] Souvatzis, P., Phonon lifetimes from first-principles self-consistent lattice dynamics, J.Phys.:Condens. Matter **23**, 445401 (2011).
[65] Monacelli, L., Bianco, R., Cherubini, M., Calandra, M., Errea, I. & Mauri, F. The stochastic self-consistent harmonic approximation: calculating vibrational properties of materials with full quantum and anharmonic effects, J.Phys.:Condens. Matter **33**, 363001 (2021).
[66] Gale, J. D., GULP: A computer program for the symmetry-adapted simulation of solids, J. Chem. Soc. Faraday Trans. **93**, 629 (1997).
[67] Plimpton, S., Fast Parallel Algorithms for Short-Range Molecular Dynamics, J. Comp. Phys. **117**, 1 (1995).
[68] Frenkel, D. Understanding Molecular Simulation : from Algorithms to Applications, San Diego:Academic Press (1996).
[69] Carrera, A., Togo, A. & Tanaka, I. DynaPhoPy: A code for extracting phonon quasiparticles from molecular dynamics simulations, Comput. Phys. Commun. **221**, 221 (2017).
[70] Eriksson, F., Fransson, E. & Erhart, P. The hiphive package for the extraction of high-order force constants by machine learning, Adv. Theory Simul. **2**, 1800184 (2019)
[71] Hellman, O., Steneteg, P., Abrikosov, I. A. & Simak, S. I. Temperature dependent effective potential method for accurate free energy calculations of solids, Phys. Rev. B **87**, 104111 (2013).
[72] Nakata, A. *et al.* Large scale and linear scaling DFT with the CONQUEST code, J. Chem. Phys. **152**, 164112 (2020).
[73] Sagotra, A. K., Chu, D. & Cazorla, C. Influence of lattice dynamics on lithium-ion conductivity: A first-principles study, Phys. Rev. Mater. **3**, 035405 (2019).
[74] Miyazaki, Y., Nakano, M., Krivchikov, A. I., Koroyuk, O. A., Gebbia, J. F., Cazorla, C. & Tamarit, J. Ll. Low-temperature heat capacity anomalies in ordered and disordered phases of normal and deuterated thiophene, J. Phys. Chem. Lett. **12**, 2112 (2021).
[75] Szewczyk, D., Gebbia, J. F., Jezowski, A., Krivchikov, A. I., Guidi, T., Cazorla, C. & Tamarit, J. Ll. Heat capacity anomalies of the molecular crystal 1-fluoroadamantane at low temperatures, Sci. Rep. **11**, 18640 (2021).
[76] Polek, A., Cazorla, C. & Kundu, D. Nature of alkali ion conduction and reversible Na-ion storage in hybrid formate framework materials, J. Phys. Chem. C **124**, 26714 (2020).
[77] Luo, X., Rawal, A., Cazorla, C. & Aguey-Zinsou, K.-F. Facile self-forming superionic conductors based on complex borohydrides surface oxidation, Adv. Sust. Sys. **4**, 1900113 (2020).
[78] Jinnouchi, R., Lahnsteiner, J., Karsai, F., Kresse, G. & Bokdam, M. Phase transitions of hybrid perovskites simulated by machine-learning force fields trained on the fly with bayesian inference, Phys. Rev. Lett. **122**, 225701 (2019).
[79] Togo, A. & Tanaka, I., First principles phonon calculations in materials science, Scr. Mater. **108**, 1 (2015).
[80] Cazorla, C., Alfé, D. & Gillan, M. J. Melting properties of a simple tight-binding model of transition metals. I. The region of half-filled *d*-band, J. Chem. Phys. **130**,

174707 (2009).
[81] Li, B. *et al.* Colossal barocaloric effects in plastic crystals, Nature **567**, 506 (2019).
[82] Bermúdez-García, J. M., Sánchez-Andújar, M. & Señarís-Rodríguez, M. A. A new playground for organic–inorganic hybrids: Barocaloric materials for pressure-induced solid-state cooling, J. Phys. Chem. Lett. **8**, 4419 (2017).
[83] Lloveras, P. *et al.*, Colossal barocaloric effects near room temperature in plastic crystals of neopentylglycol, Nat. Commun. **10**, 1803 (2019).
[84] Aznar, A. *et al.*, Reversible and irreversible colossal barocaloric effects in plastic crystals, J. Mater. Chem. A **8**, 639 (2020).
[85] Mañosa, Ll. & Planes, A. Materials with giant mechanocaloric effects: Cooling by strength, Adv. Mater. **29**, 1603607 (2017).
[86] Hull, S. Superionics: crystal structures and conduction processes, Rep. Prog. Phys. **67**, 1233 (2004).
[87] Wang, Y., Richards, W. D., Ong, S. P., Miara, L. J., Kim, J. C., Mo, Y. & Ceder, G. Design principles for solid-state lithium superionic conductors, Nat. Mater. **14**, 1026 (2015).
[88] Cazorla, C. & Errandonea, D. Superionicity and polymorphism in calcium fluoride at high pressure, Phys. Rev. Lett. **113**, 235902 (2014).
[89] Sagotra, A. K. & Cazorla, C. Stress-mediated enhancement of ionic conductivity in fast-ion conductors, ACS Appl. Mater. Interfaces **9**, 38773 (2017).
[90] Cazorla, C. In the search of new electrocaloric materials: Fast ion conductors, Res. Phys. **5**, 262 (2015).
[91] Li, W., Wu, G., Araújo, M., Scheicher, R. H., Blomqvist, A., Ahuja, R., Xiong, Z., Feng, Y. & Chen, P. Li^+ ion conductivity and diffusion mechanism in α-Li_3N and β-Li_3N, Energy Environ. Sci. **3**, 1524 (2010).
[92] Alpen, U. V., Rabenau, A. & Talat, G. H. Ionic conductivity in Li_3N single crystals, Appl. Phys. Lett. **30**, 621 (1977).
[93] Nazri, G. A., Julien, C. & Mavi, H. S. Structure of Li_3X (X = N, P, As) superionic conductors: X-ray diffraction and FTIR studies, Sol. Stat. Ionics **70**, 137 (1994).
[94] Cazorla, C. Refrigeration based on plastic crystals, Nature **567**, 470 (2019).
[95] Her, J.-H., Yousufuddin, M., Zhou, W., Jalisatgi, S. S., Kulleck, J. G., Zan, J. A., Hwang, S.-J., Bowman, R. C. & Udovic, T. J. Crystal structure of $Li_2B_{12}H_{12}$: A possible intermediate species in the decomposition of $LiBH_4$, Inorg. Chem. **47**, 9757 (2008).
[96] Lai, Q., Sun, Y., Modi, P., Cazorla, C., Demirci, U. B., Ares, J. R., Leardini, F. & Aguey-Zinsou, K. F. How to design hydrogen storage materials? Fundamentals, synthesis, and storage tanks, Adv. Sustainable Syst. **3**, 1900043 (2019).
[97] Shevlin, S. A., Cazorla, C. & Guo, Z. X. Structure and defect chemistry of low and high temperature phases of $LiBH_4$, J. Phys. Chem. C **116**, 13488 (2012).
[98] Paskevicius, M., Pitt, M. P., Brown, D. H., Sheppard, D. A., Chumphongphan, S. & Buckley, C. E. First-order phase transition in the $Li_2B_{12}H_{12}$ system, Phys. Chem. Chem. Phys. **15**, 15825 (2013).
[99] Mohtadi, R. & Orimo, S. I. The renaissance of hydrides as energy materials, Nat. Rev. Mater. **2**, 16091 (2016).
[100] Sau, K., Ikeshoji, T., Kim, S., Takagi, S., Akgi, K. & Orimo, S.-I. Reorientational motion and Li^+ ion transport in $Li_2B_{12}H_{12}$ system: Molecular dynamics study, Phys. Rev. Mater. **3**, 075402 (2019).
[101] Verdal, N., Her, J.-H., Stavila, V., Soloninin, A. V., Babanova, O. A., Skripov, A. V., Udovic, T. J. & Rush, J. J. Complex high-temperature phase transitions in $Li_2B_{12}H_{12}$ and $Na_2B_{12}H_{12}$, J. Sol. Stat. Chem. **212**, 81 (2014).
[102] Udovic, T. J., Matsuo, M., Unemoto, A., Verdal, N., Stavila, V., Skripov, A. V., Rush, J. J., Takamura, H. & Orimo, S.-I. Sodium superionic conduction in $Na_2B_{12}H_{12}$, Chem. Commun. **50**, 3750 (2014).
[103] Jorgensen, M., Shea, P. T., Tomich, A. W., Varley, J. B., Bercx, M., Lovera, S., Cerny, R., Zhou, W., Udovic, T. J., Lavallo, V., Jensen, T. R., Wood, B. C. & Stavila, V. Understanding superionic conductivity in lithium and sodium salts of weakly coordinating closo-hexahalocarbaborate anions, Chem. Mater. **32**, 1475 (2020).
[104] Zhang, L. *et al.*, Giant polarization in super-tetragonal thin films through interphase strain, Science **361**, 494 (2018).
[105] Yamada, H. *et al.*, Giant electroresistance of super-tetragonal $BiFeO_3$-based ferroelectric tunnel junctions, ACS Nano **7**, 5385 (2013).
[106] Infante, I. C. *et al.*, Multiferroic phase transition near room temperature in $BiFeO_3$ films, Phys. Rev. Lett. **107**, 237601 (2011).
[107] Yamamoto, H., Ogata, T., Saki, Y. & Azuma, M. Stability of polar structure in filling-controlled giant tetragonal perovskite oxide $PbVO_3$, Inorg. Chem. **58**, 2755 (2019).
[108] Pan, Z. *et al.*, Large negative thermal expansion induced by synergistic effects of ferroelectrostriction and spin crossover in $PbTiO_3$-based perovskites, Chem. Mater. **31**, 1296 (2019).
[109] Belik, A. A. *et al.*, Neutron powder diffraction study on the crystal and magnetic structures of $BiCoO_3$, Chem. Mater. **18**, 798 (2006).
[110] Wang, J. *et al.*, Epitaxial $BiFeO_3$ multiferroic thin film heterostructures, Science **299**, 1719 (2003).
[111] Menéndez, C. & Cazorla, C., Giant thermal enhancement of the electric polarization in ferrimagnetic $BiFe_{1-x}Co_xO_3$ solid solutions near room temperature, Phys. Rev. Lett. **125**, 117601 (2020).
[112] Bowen, C. R., Taylor, J., LeBoulbar, E., Zabek, D., Chauhan, A. & Vaish, R. Pyroelectric materials and devices for energy harvesting applications, Energy Environ. Sci. **7**, 3836 (2014).
[113] Hoffmann, M., Schroeder, U., Künneth, C., Kersch, A., Starschich, S., Böttger, U. & Mikolajick, T. Ferroelectric phase transitions in nanoscale HfO_2 films enable giant pyroelectric energy conversion and highly efficient supercapacitors, Nano Energy **18**, 154 (2015).
[114] Gottschall, T. *et al.*, A multicaloric cooling cycle that exploits thermal hysteresis, Nat. Mater. **17**, 929 (2018).
[115] Menéndez, C. & Cazorla, C., Colossal room-temperature electrocaloric strength aided by hydrostatic pressure in multiferroic $BiFe_xCo_{1-x}O_3$ solid solutions, To be published (2022).
[116] Hojo, H., Kengo, O., Keisuke, S., Yamamoto, H., Kawabe, R. & Azuma, M. Development of bismuth ferrite as a piezoelectric and multiferroic material by cobalt substitution, Adv. Mater. **30**, 1705665 (2018).